Materials Characterization 197 (2023) 112692

Contents lists available at ScienceDirect

Materials Characterization

journal homepage: www.elsevier.com/locate/matchar

Grain scale residual stress response after quasi-static and high strain rate loading in SS316L

Sven E. Gustafson [a], Darren C. Pagan [b], Brett Sanborn [c], Michael D. Sangid [a,*]

[a] *School of Aeronautics and Astronautics, Purdue University, West Lafayette, IN, USA*
[b] *Pennsylvania State University, University Park, PA, USA*
[c] *Sandia National Laboratories, Albuquerque, NM, USA*

ARTICLE INFO

Keywords:
Residual stress
High energy x-ray diffraction microscopy
Lattice reorientation
Intragranular deformation

ABSTRACT

High strain rate applications for stainless steels are common, from material processing to ballistics, and residual stresses generated within components during these applications can influence their future performance. Here, high energy x-ray diffraction is employed to examine the development of grain scale residual stress and lattice reorientation under different applied strain rates in an austenitic stainless steel (SS316L). High energy x-ray diffraction was performed before and after loading on specimens deformed at both high and quasi-static strain rates. These measurements show a larger spread in grain averaged residual stresses in the specimen deformed at high strain rate, while the grain averaged reorientation, a metric of plastic strain, was larger in the specimen deformed quasi-statically. Electron backscatter diffraction, employed post-deformation to further investigate the effect of strain rate upon the specimens, found no distinct difference in intragranular misorientation between the two loading conditions. Here it is postulated that the lower deformation rates during the quasi-static test provided more time for crystallographic slip to occur. With greater time, local plasticity through increased, measured lattice reorientation (facilitated by grain boundaries acting as defect sinks) lead to the presence of lower quantities of residual stresses upon unload of the quasi-static test compared to the high strain rate test.

1. Introduction

Structural alloys exhibit a well-known strain rate dependent response. In high strain rate regimes, encountered during manufacturing processes or impact loading, marked differences in an alloy's strength and hardening response are observed as compared to static/quasi-static loading [1]. Therefore, it is of interest to explore the differences between the various loading regimes especially on the microscale, where the culmination of grain scale evolution leads to said observed differences at the macroscopic level. Metrics to explore these differences, such as residual stress, have themselves a stark impact upon the performance of such materials and can limit component lifetimes. However, there is a missing connection between the measured grain scale residual stress and deformation metrics across applied strain rate regimes. Thus, this work uses high energy x-rays, ex-situ loading, and post-deformation electron backscatter diffraction (EBSD) to investigate the grain scale differences between quasi-static (QS) and high strain rate (HSR) loading in stainless steel 316L (SS316L), which is used widely for its corrosion resistance and strength at high temperatures, to illuminate the potential impact upon material behavior.

The deformation behavior of structural alloys are such that the degree of material response is a function of the applied strain rate [2]. This work's focus is on two specific strain rates in SS316L, with a QS and a HSR of 10^{-4} and 10^{2}, respectively. For SS316L, in the QS regime ($10^{-4} - 10^{-1}\ s^{-1}$), the material's mechanical properties, such as yield stress, vary relatively little with the logarithm of strain rate. At higher strain rates ($10^{2} - 10^{6}\ s^{-1}$), as seen during processing, impact, and ballistics, its properties are significantly more strain rate sensitive [3]. Testing of structural metals under QS loading, to determine material properties for use in static load calculations, can be completed on standard servo-hydraulic load frames (upper strain rate limit $\sim 10^{-1}\ s^{-1}$). The intermediate strain rate range ($10^{0} - 10^{2}\ s^{-1}$) has been historically difficult to characterize due to experimental difficulties associated with load frame stiffness and ringing effects related to the measurement of force histories; however, specialized loading systems such as high-rate servo-hydraulics and Drop-Hopkinson bars are designed to characterize this range [4,5]. Higher strain rate testing requires specific equipment, such as the split Hopkinson (Kolsky) bar and its many adaptations [6,7] to

---

* Corresponding author at: 701 W. Stadium Ave. West Lafayette, IN 47907-2045, USA.
E-mail address: msangid@purdue.edu (M.D. Sangid).

https://doi.org/10.1016/j.matchar.2023.112692
Received 17 September 2022; Received in revised form 14 January 2023; Accepted 16 January 2023

match the strain rates seen during impact or machining ($10^2\ s^{-1}$) and ballistics ($10^4\ s^{-1}$). Interrupted loading of high rate tensile experiments with Kolsky bars has received sparse attention in the past, and has been limited to relatively large strains due to difficulties controlling the total amount of strain applied [8].

Investigations of SS316L, and similar austenitic stainless steels such as SS304L, have been conducted to characterize the material's response across strain rates. Past works have shown an increase in localized grain deformation and higher dislocation density at higher strain rates [3,9]. These past results were observed for strain rates in the intermediate to high regimes and a recent EBSD study on a solution annealed SS304LN by Kundu et al. [10] showed a similar trend of increasing dislocation density with strain rate even within the low strain rate regime ($10^{-4} - 10^{-2}\ s^{-1}$). A work by Acharya et al. [11] recently showed increased strain localization, which is a well-known precursor to crack initiation [12], with an increased strain rate along with microcracks initiating at junctions of two slip-bands or slip-bands and grain boundaries. It is noted that these previous works employ electron microscopy to visualize deformation localization within the microstructure and EBSD to expose dislocation densities and orientation deviations.

Along with microstructural differences, stress metrics, such as the flow and yield stresses, have been shown to increase with strain rate. Lee et al. investigated a sintered SS316L over strain rates ranging from $10^{-3}\ s^{-1}$ to $7.5x10^3\ s^{-1}$ and found that the flow stress varies linearly with the log of strain rate, but is broken into two distinct bilinear regimes where, after a transition strain rate around $1.1x10^3\ s^{-1}$, the flow stress begins to increase dramatically with increasing strain rate (displaying a higher slope of the linear function) [3]. A similar trend was also seen in SS304L [9]. This transition in deformation behavior, where the flow stress of the material as a function of strain rate beings to increase around strain rate $10^3\ s^{-1}$, is associated with an increase in dislocation generation, which subsequently increases the number of barriers preventing thermally activated dislocation motion [13,14]. Jin et al. [15] recently characterized the entirety of the strain rate range, including the intermediate strain rates on a SS304L-VAR, and showed that the material's response deviates from the standard linear relationship between stress and the logarithm of strain rate beginning in the intermediate strain rate range, below $10^3\ s^{-1}$. Additionally, these studies show that the yield stress of the material increases with strain rate and the study by Kundu et al. [10], which observed a yield stress increase even in the lower strain rates, attributed this to the requirement of a higher applied stress to maintain a higher dislocation velocity. However, these studies only explore flow stress on the macroscopic scale and are unable to probe the grain scale stresses, in particular the techniques employed do not capture the variation of stresses from grain to grain in the material.

At the continuum scale, the presence of tensile or compressive residual stresses within a structural metal has been linked to a detrimental or beneficial, respectively, response in fatigue, fracture, and corrosion [16–19]. Explorations into residual stress often study component scale stresses (Type 1) at or near the surface of the material and determine their impact upon the material's lifetime, but interest also exists in investigating the grain scale stresses (Type 2) within the material. High energy x-ray diffraction microscopy (HEDM) allows for the characterization of grain scale elastic strains (which can be associated to grain averaged stress tensors with knowledge of the single crystal elastic constants) within a polycrystalline material [20–22]. Chatterjee et al. [23] identified and quantified a significant residual stress on the grain scale due to local plastic yielding and examined the rationale for a grain to change from a tensile to compressive stress state during unloading based on the triaxiality and slip character of the grain neighborhood. Further, a study by Kapoor and Sangid initialized residual stresses obtained from HEDM within crystal plasticity simulations, which notably influenced the local material response and therefore indicates the importance of including residual stresses when predicting material failure [24]. Explorations into the effect of strain rate upon the residual stress, particularly Type 2, have been limited: a study by Tiwari et al. [25] in copper showed that an increasing Type 1 residual stress was seen with an increase in strain rate; however, as noted within the study, the measurements were over a limited range of strain rates ($0.01 - 0.6\ s^{-1}$) and below the strain rates seen during material processing.

In an effort to further explore the link between residual stress, material deformation, and strain rate, this study will capture Type 2 residual stresses before and after deformation in both a quasi-statically loaded specimen and a high strain rate loaded specimen. Such information will provide insight into the (potentially detrimental) residual stresses in polycrystal materials during forming, machining, or impact loading. In this work, HEDM and post-deformation EBSD is used on SS316L specimens loaded ex-situ to a final plastic strain of ~2% via quasi-static and high strain rates of $10^{-4}\ s^{-1}$ and $10^2\ s^{-1}$, respectively, to investigate the effect of strain rate upon grain scale deformation metrics and grain scale residual stress.

2. Material and loading configuration

A stainless-steel alloy commonly used in industries ranging from nuclear to biomedical, SS316L, was chosen for this experiment. Stock material was purchased from Goodfellow and annealing heat treatments were trialed to produce a uniform, large grain size (~90 μm average grain diameter) to ensure the microstructure was suitable for HEDM characterization [22]. The resulting heat treatment was 1100 ° *C* for 85 *min*. After processing, tensile specimens with square cross sections of 1 mm^2 and gauge length of 8 *mm* were extracted via electrical discharge machining (EDM) as shown in Fig. 1b. These specimens were designed for mechanical loading and high energy x-ray interrogation in the rotational and axial motion system (RAMS) [26].

For comparison, two specimens were deformed targeting the same overall applied strain, one quasi-statically and one at high strain rate. The QS specimen was loaded with an applied strain rate of approximately $1x10^{-4}\ s^{-1}$, in the RAMS screw-driven load frame. The specimen was displaced under constant velocity with ten interrupted load steps to conduct x-ray characterization. Prior to each HEDM scan, the specimen was displaced to reduce the load on the specimen by ~20% to avoid macroscopic stress relaxation during the ~40 minute HEDM scan. The macroscopic strain within the HEDM interrogation region was calculated during QS loading using digital image correlation (DIC) performed on optical images of the specimen surface and tracked the average strain from the fine surface roughness features from EDM machining. For simplicity, the interrupted, in situ HEDM scans were not included in this work and as such the load drops were removed from the loading profile in Fig. 1a. After loading, the total strain imparted to the QS specimen

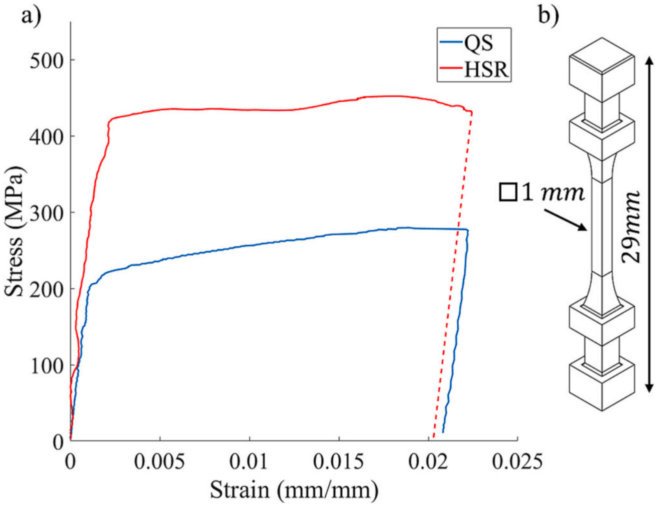

Fig. 1. a) Engineering stress vs engineering strain curves for the QS (strain rate of 10^{-4}) and HSR (strain rate of 10^2) specimens. b) Specimen design.

was approximately 2.08% as measured by DIC. The loading of the HSR specimen was conducted using a modified Kolsky tension bar specially designed for this test to allow single loading of a specimen loaded to small strains (2.03%). The specimen was loaded using this technique at a strain rate of approximately 100 s^{-1}. Owing to the complexity of the specimen geometry and indirect displacement measurement technique, a finite element (FE) analysis was conducted, and a strain correction method was developed to determine an accurate final strain applied to the HSR specimen. A detailed description of the experimental setup and test process, as well the strain correction method, is presented in Appendix A.

The macroscopic stress-strain curves for the QS and HSR specimens are shown in Fig. 1a, in which there is a marked, expected difference in behavior. The yield stress of the HSR specimen, roughly 420 *MPa*, is twice that of the QS specimen, roughly 210 *MPa*. This increase in yield stress with the strain rate is an expected consequence of the increased strain rate sensitivity of stainless steel [15]. With the correction, derived from a FE model, applied to the HSR stress/strain data, the stiffnesses of the QS and HSR tests, are roughly 193 *GPa* and 198 *GPa* respectively. For the QS specimen, the unloaded total strain of the interrogation region, as determined by DIC, was 2.08%; whereas the unloaded total strain of the HSR specimen, as calculated using the correction detailed in Appendix A, was 2.03%. Due to the difficulty of loading to a specific final total strain during HSR tests, the difference, 0.05%, is within expectations.

3. Characterization

HEDM is a high energy x-ray technique which rotates a polycrystalline material and collects diffracted signal upon downstream area detectors when individual crystalline volumes satisfy Bragg's law (depicted in Fig. 2 where ω is the rotation about the axis aligned with the loading axis of the specimen) [20]. The two primary modalities of HEDM are near field (NF-HEDM) and far field (FF-HEDM) which are distinguished by their detector distances [27,28]. NF-HEDM, with a detector placed <10 *mm* from the specimen, collects individual grain's diffracted signal with high spatial resolution to allow for reconstructions of spatially distributed orientation volumes, where each grain and its morphology is determined, as shown in Fig. 3. FF-HEDM, with a detector placed roughly 1000 *mm* from the specimen (800 *mm* here), collects the diffracted signal from each grain with high angular resolution which allows for reconstructions of the grain averaged orientation, centroid, and elastic strain tensor. The grain averaged orientation and elastic strain resolutions of FF-HEDM have been estimated to be 0.01° and 10^{-4}, respectively [28,29].

The data for this study was collected during three separate beamtimes, at three separate beamlines, each at the Cornell High Energy Synchrotron Source (CHESS), with a beam energy of 61.332 *keV*. The HSR specimen was first scanned in its undeformed state at the F2 beamline, then later scanned after ex-situ deformation at the 1A3 beamline. The QS specimen was scanned entirely at the 3A beamline. NF-HEDM was completed using a LuAg:Ce scintillator coupled with an 5*x* objective lens attached to a Retiga 4000 DC CCD camera with 2048 *x* 2048 pixels and an effective pixel size of 1.48 μm. The NF-HEDM detector working distances for each of the experiments at F2, 1A3, and 3A were 6.82, 6.12, and 6.46 *mm* respectively. FF-HEDM was completed using two Dexela 2923 area detectors with 3888 *x* 3072 pixels with an effective pixel size of 74.8 μm. For FF-HEDM, the working distances at each beamline were 877, 859, and 731 *mm* respectively. For both specimens during the undeformed NF-HEDM scanning, data was collected for six, 170 μm tall boxes with 10 μm overlap between boxes leading to a 900 μm tall interrogation region. FF-HEDM was collected in these six regions as well as two 'padding' boxes above and below. For the deformed states, NF-HEDM was only collected for the interior four boxes. Reconstructions for each box were performed in HEXRD [28] and later assembled in an in-house MATLAB script. Three beamtimes were necessary to allow for ex-situ loading which, due to physical upgrades occurring at CHESS, required three separate beamlines. Calibrants scanned at the start of each beamtime were used to minimize systematic discrepancies due to differences in experimental set-ups. The same calibration methodology was used for each experiment and subsequent

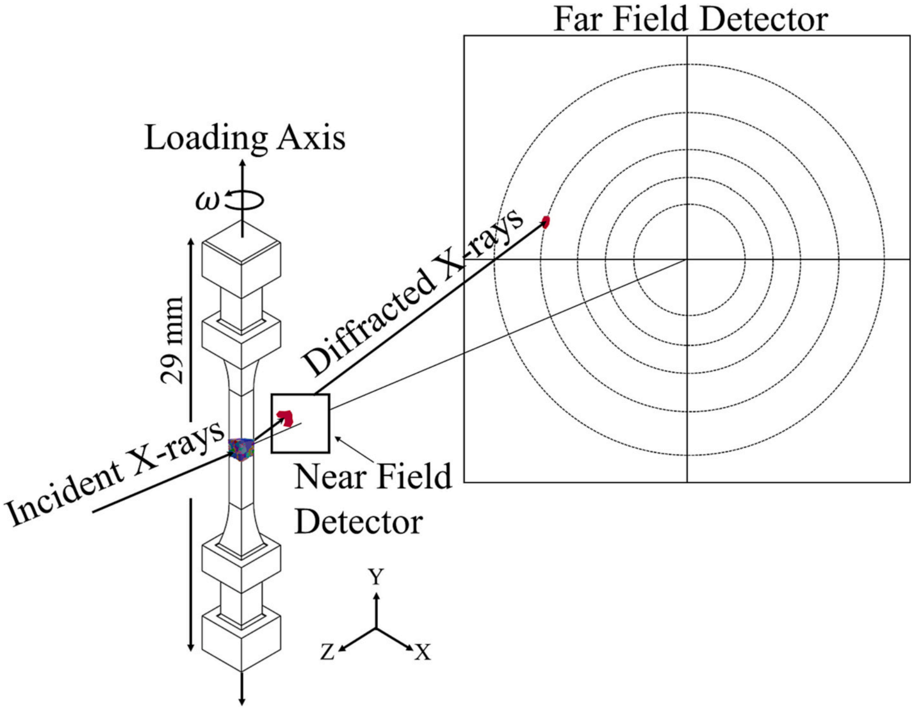

Fig. 2. HEDM schematic demonstrating a rotating specimen and position of the near field and far field detectors to capture the diffracting x-ray signal. A single illustrative diffraction peak is shown in red upon both the near field and far field detectors. (For interpretation of the references to colour in this figure legend, the reader is referred to the web version of this article.)

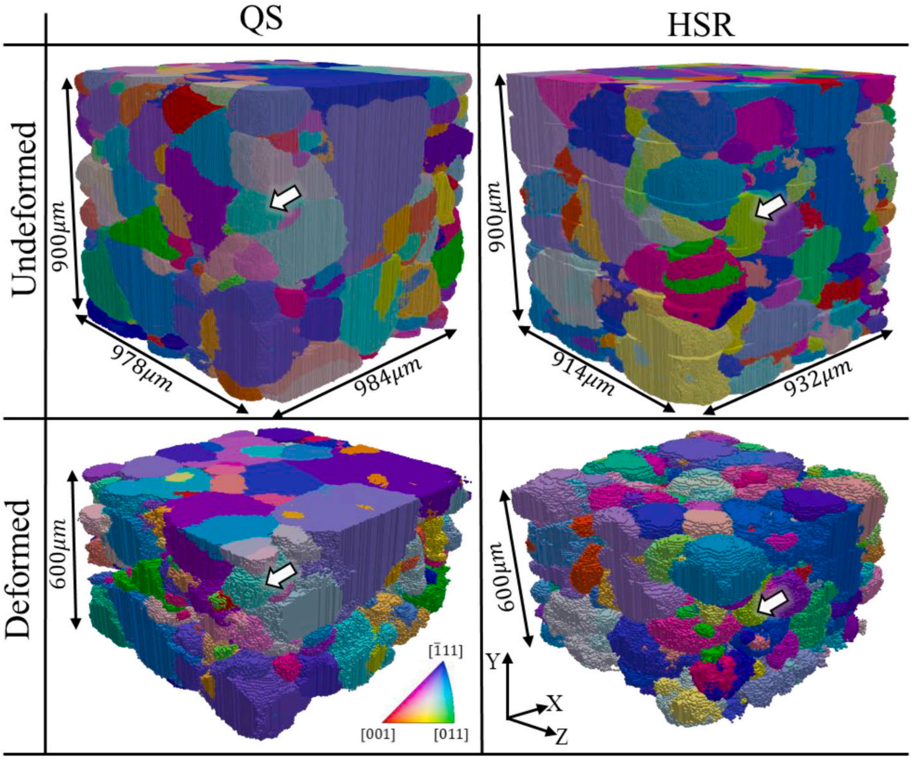

Fig. 3. Undeformed and deformed NF-HEDM reconstructions (shown in rows) for the QS and HSR samples (shown in columns). The white arrows serve as fiducial marks to visually track selected grains between the undeformed and deformed states.

reconstructions. After reconstruction, via knowledge of the single crystal stiffness values, $[C_{11}, C_{12}, C_{44}] = [206, 133, 119]$ *GPa* [22,30] for this material, the elastic strain tensors of each grain from FF-HEDM were converted into stress tensors using the anisotropic form of Hooke's law for cubic materials as shown in Eq. 1:

$$\sigma_{ij} = C_{ijkl}\varepsilon_{kl} \tag{1}$$

where σ_{ij} is the stress tensor, ε_{kl} is the elastic strain tensor from FF-HEDM, and C_{ijkl} is the fourth-order stiffness tensor with symmetry for cubic materials [20]. Prior to performing any subsequent analysis on the residual stress state of the unloaded sample, any mean stresses or moments due to specimen gripping were removed. The inclusion of any mean stress or bending moment did not alter the findings of this study; no spatial dependency of spread in residual stress was observed on either specimen. Rotational registration of the HSR microstructures before and after loading was performed using an optimization routine in MATLAB which minimized the misorientation between the orientations in each reference frame (undeformed and deformed) of eight, random yet known grains simultaneously. By applying the determined angle as a rotation to the deformed grains across the entire interrogation volume, the specimen fames were aligned for subsequent analysis. To ensure a one-to-one match between undeformed and deformed grains, manual matching was completed by comparing pre and post deformation NF-HEDM for both specimens; only grains which were successfully matched with high confidence were considered for analysis in this work.

The NF-HEDM results are shown in Fig. 3 where both specimens are displayed in the undeformed and deformed states. The undeformed reconstructions were completed with a voxel size of 2 μm to maximize accuracy of defining the grain boundaries, while the deformed states were reconstructed with a coarser 5 μm voxel due to challenges reconstructing grains with elevated dislocation content using NF-HEDM. Each volume in Fig. 3 shows only voxels with a reconstruction confidence (ratio between measured and predicted intensity of a given orientation) of at least 0.5. The overall confidence across the reconstructions of the undeformed specimens is higher than of the deformed specimens, capturing the regions near grain boundaries well. The white arrows in Fig. 3 point to a single grain, serving as a fiducial mark, that can be used to track the undeformed to the deformed states. The NF-HEDM reconstructions are completed with grain averaged orientations determined from FF-HEDM for each grain, thus removing any intragranular misorientation that may be present within the grains [31]. The poor confidence values in the NF-HEDM reconstruction of the deformed specimens are likely due to deviations from the grain averaged orientation or localized disruptions in the crystallinity of the lattice.

The NF-HEDM reconstruction method employed was unable to reconstruct intragranular lattice misorientation. To probe this information, EBSD was later conducted post-deformation to investigate the spatial localization of deformation within grains. After data collection from HEDM, the two specimens were cross-sectioned through the gauge section via EDM, mounted, polished, and then imaged. The EBSD analysis was performed on a spatially representative region in the gauge section of each specimen, but was not spatially linked to the NF-HEDM region of interest. Post-deformation imaging and subsequent EBSD data collection was conducted within a FEI Quanta 650 FEG scanning electron microscope with a working distance of 15 *mm*, specimen tilt of 70°, and energy of 15 *keV*. EBSD was collected on an EDAX system with a 1 μm step size and field of view of approximately the entire cross section; the data was later cropped to avoid polishing inconsistencies around the specimen boundaries. Data was initially collected in TSL OIM Analysis software package then final analysis was completed in MATLAB via the MTEX [32] crystallography toolbox. Fig. 4 shows inverse pole figures of the cross sections of the two specimens after deformation. The kernel averaged misorientation (KAM) plots, shown in Fig. 7, were completed with an order of $n = 3$ and ignore misorientation values larger than 1°. The grain reference orientation deviation (GROD) plots, also in Fig. 7, were completed with respect to the grain averaged orientation. KAM is a metric of local neighborhood misorientation while GROD is a metric of each points deviation from the grain averaged orientation [33].

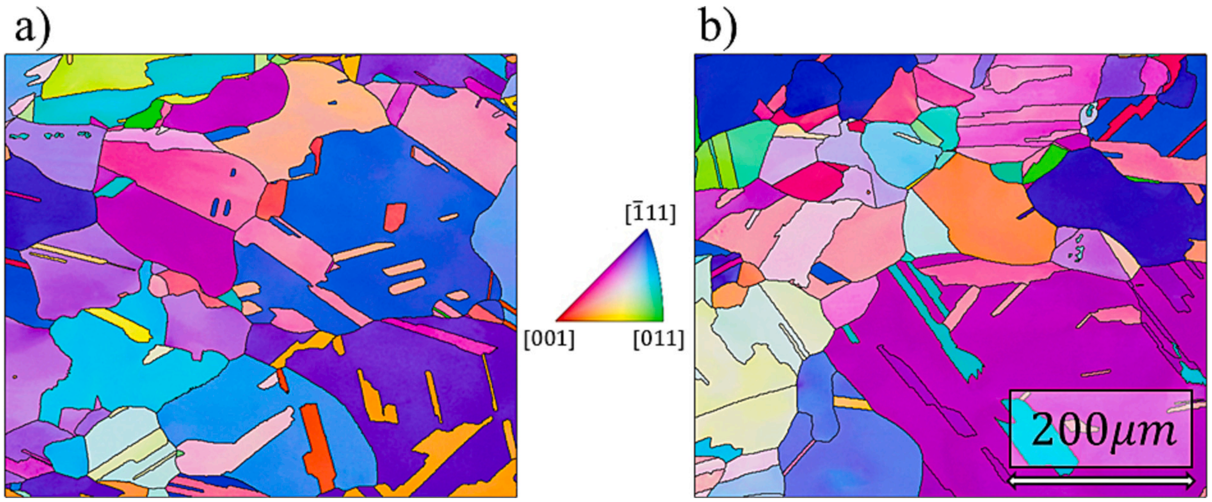

Fig. 4. EBSD of the deformed a) QS specimen and b) HSR specimen.

4. Results and discussion

The first deformation metric examined in the specimens is the grain averaged lattice reorientation. This value is calculated based on the FF-HEDM lattice orientation measurements of the grains before and after deformation. For polycrystalline alloys, crystallographic slip results in a plastic spin [34], which in turn produces lattice rotation as grains attempt to maintain compatibility and satisfy local boundary conditions. Fig. 5 shows the grain averaged reorientation for the QS and HSR specimens, as well as a cumulative distribution function comparing the two simultaneously. Fig. 6 shows the orientation change, with minimal texture evolution, of each grain in both the QS and HSR samples. In Fig. 5a and b, it can be seen that the grain average reorientation distribution of the QS specimen appears greater than the HSR, both in terms of average and spread. Additionally, from a two sample *t*-test, the QS specimen (M = 0.83°, SD = 0.44°) exhibited a larger mean reorientation than the HSR specimen (M = 0.72°, SD = 0.42°), by a statistically significant margin (t(697) = −3.30, $p < 0.01$), where t is the T-statistic which is significant for a *p*-value, p, with df degrees of freedom. All statistical tests were performed in MATLAB with a statistical significance, α, level of 0.01; M and SD are the mean and standard deviation respectively. The QS reorientation mean, is greater than the HSR mean by 0.11°, or an increase of about 15%, while the difference in macroscopic total strain of the two tests is relatively small, 0.05%, or an increase of about 2%. With the difference in total strain considered, the QS specimen demonstrates a demonstratively larger amount of lattice reorientation than the HSR specimen.

To examine the intragranular misorientation differences between the two deformed microstructures, EBSD analysis was performed on both specimens post deformation. Fig. 7 shows the KAM and GROD for both the QS and HSR specimens after deformation. Visually there appears to be little difference between the two strain rates from the EBSD; however, via a statistical analysis it was found that the mean KAM of the QS case (M = 0.24°, SD = 0.087°), was larger than that of the HSR case (M = 0.21°, SD = 0.086°) by a statistically significant margin (t(563622) = −100.26, $p < 0.01$). While the difference in mean KAM between the two strain rates is relatively small, it does show that there is a slightly higher amount of KAM within the QS case which is consistent with the small difference in macroscopic total strain between the specimens (as demonstrated in Fig. 1a), similar to the grain averaged reorientation. Das et al. [35] found that the average KAM did increase with strain rate in a dual-phase steel; however, this increase was not significant until strain rates approaching $10^3\ s^{-1}$ which gives support to the lack of substantial difference between KAM seen here. Investigating the GROD plots, the HSR specimen held a larger mean (M = 0.013°, SD = 0.0076°), than the QS specimen (M = 0.0012°, SD = 0.0070°), by a statistically significant margin (t(563626) = 29.45, $p < 0.01$). However, the GROD plots in Fig. 7 do show clear localization of misorientation at grain

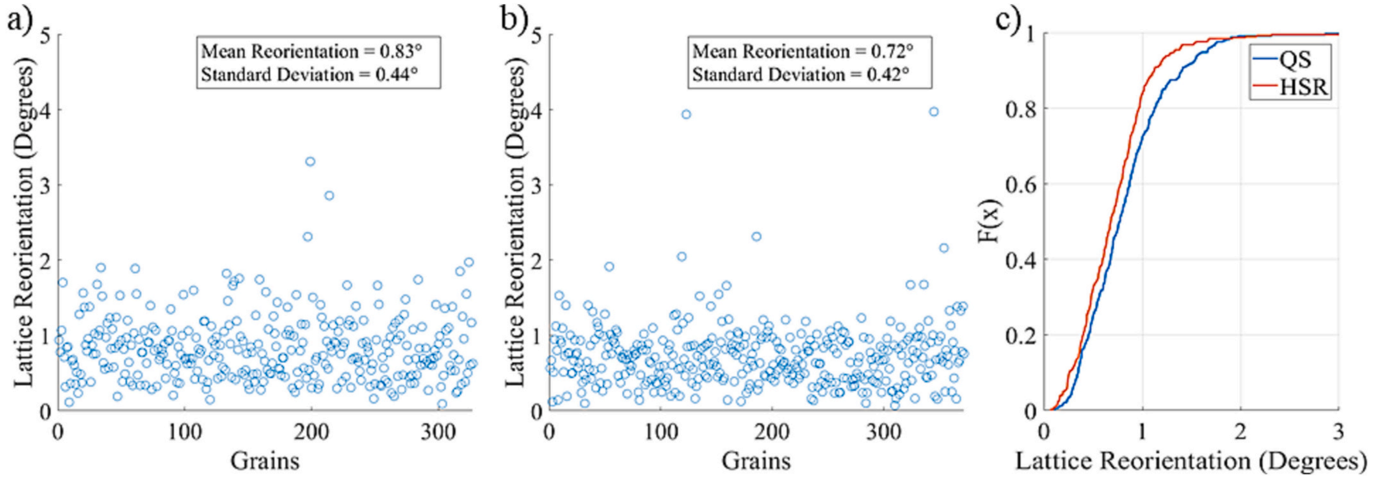

Fig. 5. Grain averaged lattice reorientation between the undeformed and deformed states for the a) QS and b) HSR specimens, while c) shows the cumulative distribution functions of both data sets.

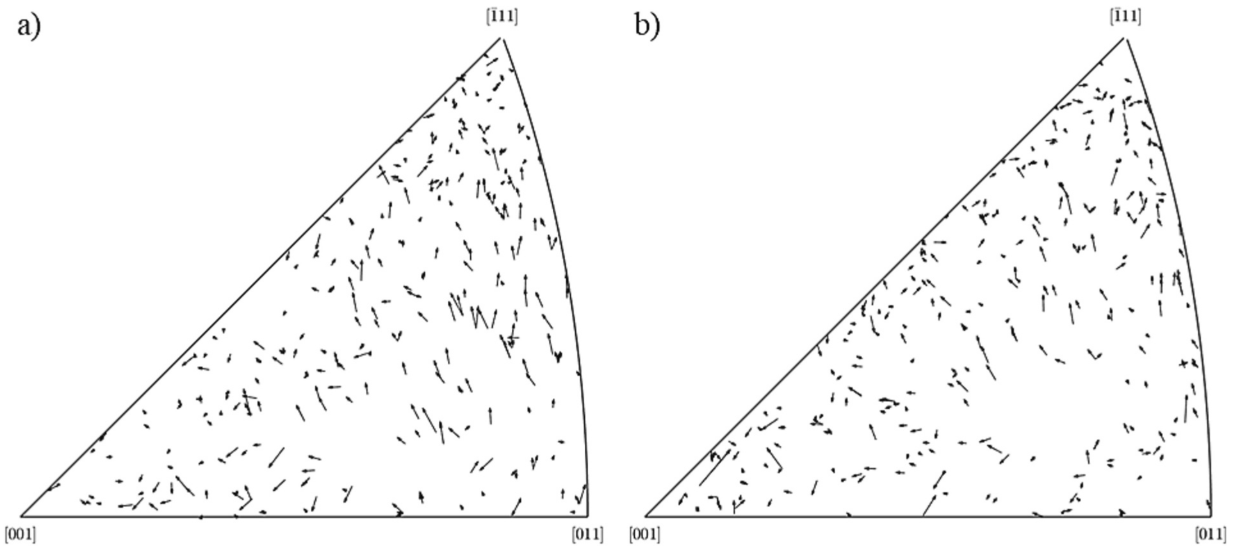

Fig. 6. Individual orientation change for each grain in the a) QS and b) HSR specimens between the undeformed and deformed loading states. Plot is inverse pole figure where each arrow points from the undeformed orientation to the deformed orientation.

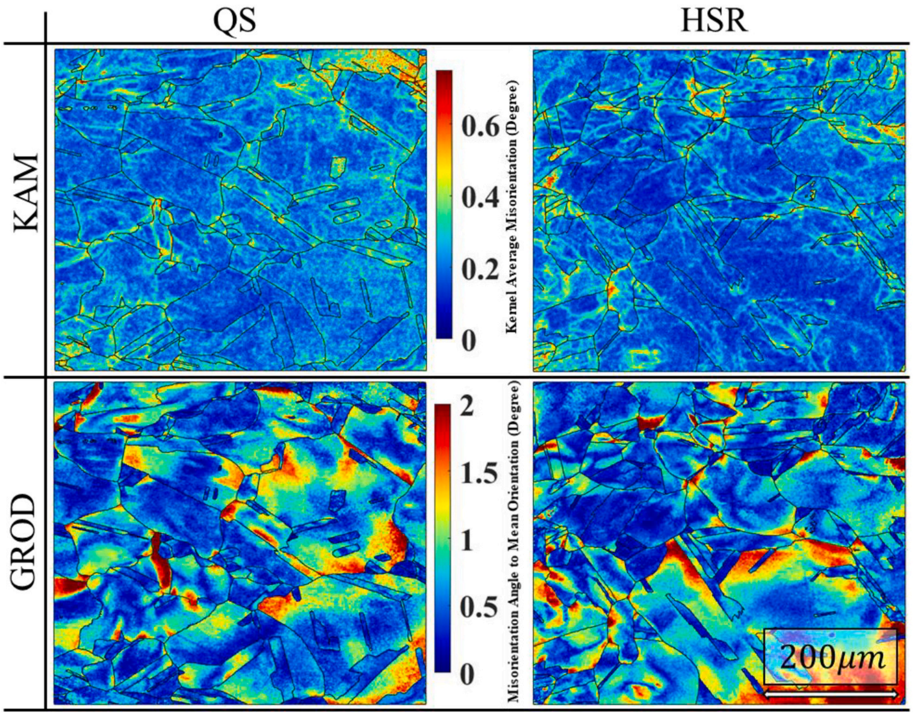

Fig. 7. Two metrics of intragranular misorientation are shown from the EBSD data in Fig. 4. Kernel averaged misorientation (KAM) is a metric of local neighborhood misorientation. Grain reference orientation deviation (GROD) is a metric of each points deviation from the mean grain orientation. In each case, the misorientation is more localized near the grain boundaries.

boundaries in both specimens. While the KAM plot does not appear to indicate that distinct sub-grain regions have formed as the specimens were only tested to 2% final total strain, the GROD plots agree with the deformed NF-HEDM in Fig. 3 to show that a single grain averaged orientation no longer characterizes the entire grain. Values in both specimens approach 2° in deviation from the average orientation, especially at grain boundaries, displaying clear indications of deformation localization in those areas and the beginnings of sub-grain formation. By investigating all possible orientations contained within a single grain as defined by FF-HEDM [36], misorientation from the grain averaged orientation were seen to approach 3°, confirming the existence of heavily misorientated regions within the grain while still within the bulk polycrystal, prior to specimen cross-sectioning (Appendix B). Both specimens showed equal tendency for misorientation localization from EBSD and the results indicate that there is not a demonstrative difference in the intragranular misorientation values for the QS and HSR specimens.

The FF-HEDM measurements also extract the full elastic strain tensor of the grains in each specimen, which were used to calculate the residual stresses prior to and post deformation. Fig. 8 shows the grain averaged stress metrics with mean stresses removed to allow focused presentation of residual stress distributions for both specimens in the undeformed and

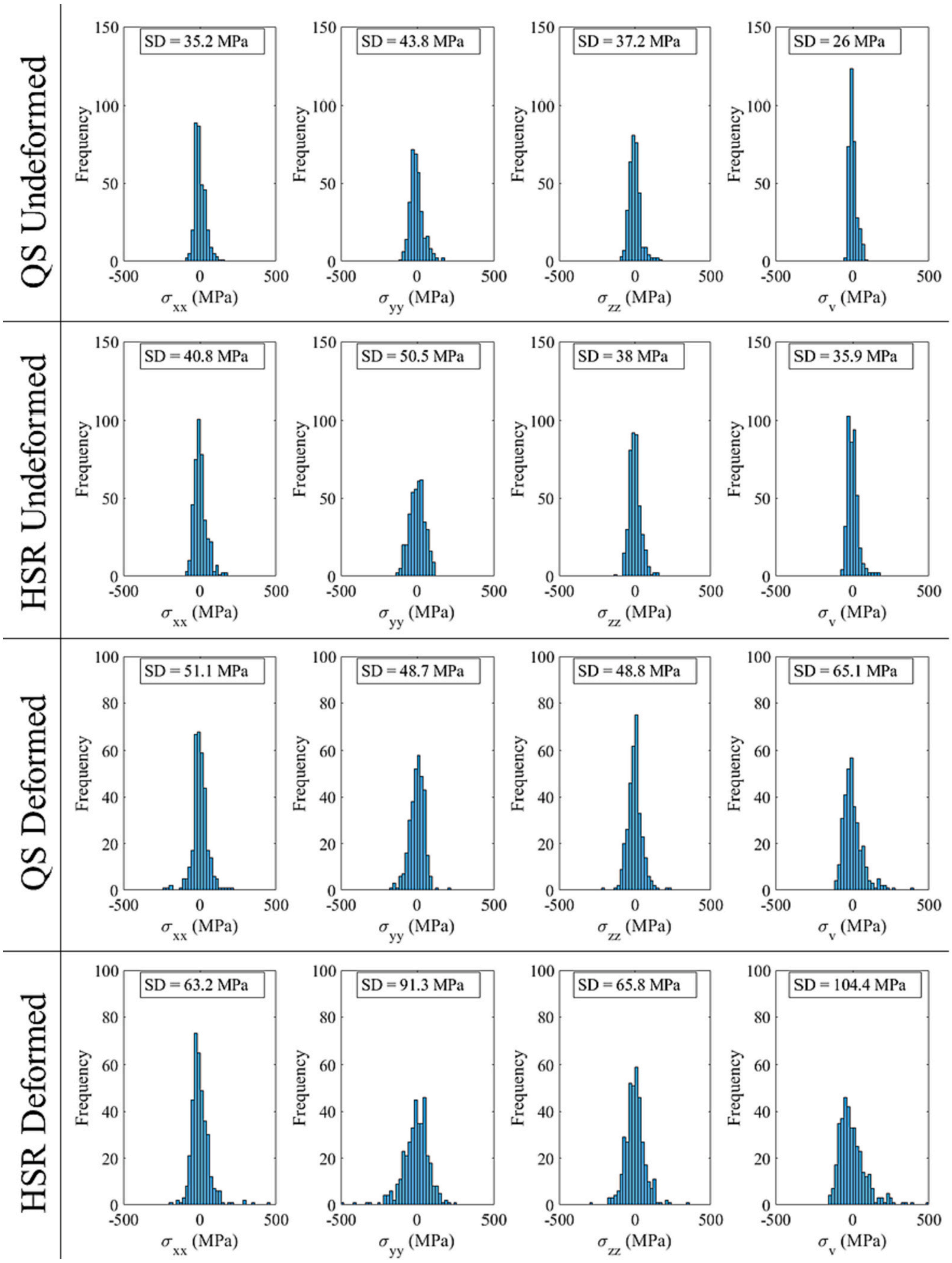

Fig. 8. Grain averaged residual stress distributions for both strain rates and deformation states. Stress metrics shown include the von Mises stress (σ_v) and the normal stresses (σ_{xx}, σ_{yy}, σ_{zz}), where Y is the loading axis. SD is the standard deviation of each residual stress distribution.

deformed condition. Both specimens begin with relatively similar distributions of residual stresses within the specimen as shown in the top two rows of Fig. 8. Note that these specimens were well annealed to minimize residual stresses within the undeformed material. After deformation however, there are differences in the residual stress distributions between the two loading regimes. Fig. 8 shows that the QS loading minimally altered the residual stress distribution within the specimen throughout deformation with the standard deviation of the stress along the loading direction before and after loading of 43.8 MPa and 48.7 MPa, respectively. Fig. 8 also shows that the standard deviation of the grain averaged stresses along the loading direction nearly doubled during deformation of the HSR specimen from 50.5 MPa and 91.3 MPa, respectively. The transverse normal residual stress distributions of the HSR specimen were also seen to increase, though less than the stress along the loading direction. Via a two sample F-test a statistically significant difference was found between the stress distributions along the loading direction; the spread (variance) of the deformed HSR stresses was shown to be greater than that of the deformed QS specimen ($f(371,326) = 3.51, p < 0.01$), where f is the F-statistic which is significant for a p-value, p, with HSR and QS degrees of freedom represented as df1 and df2, respectively. As seen from the large difference in standard deviations, the HSR specimen now contains more grains with extreme stress values. To better demonstrate these higher magnitude values, Fig. 9 shows the residual stress along the loading direction of each individual grain for both strain rates and deformation states. In Ti and Ni-based alloys, the envelope of grain averaged stress states has been

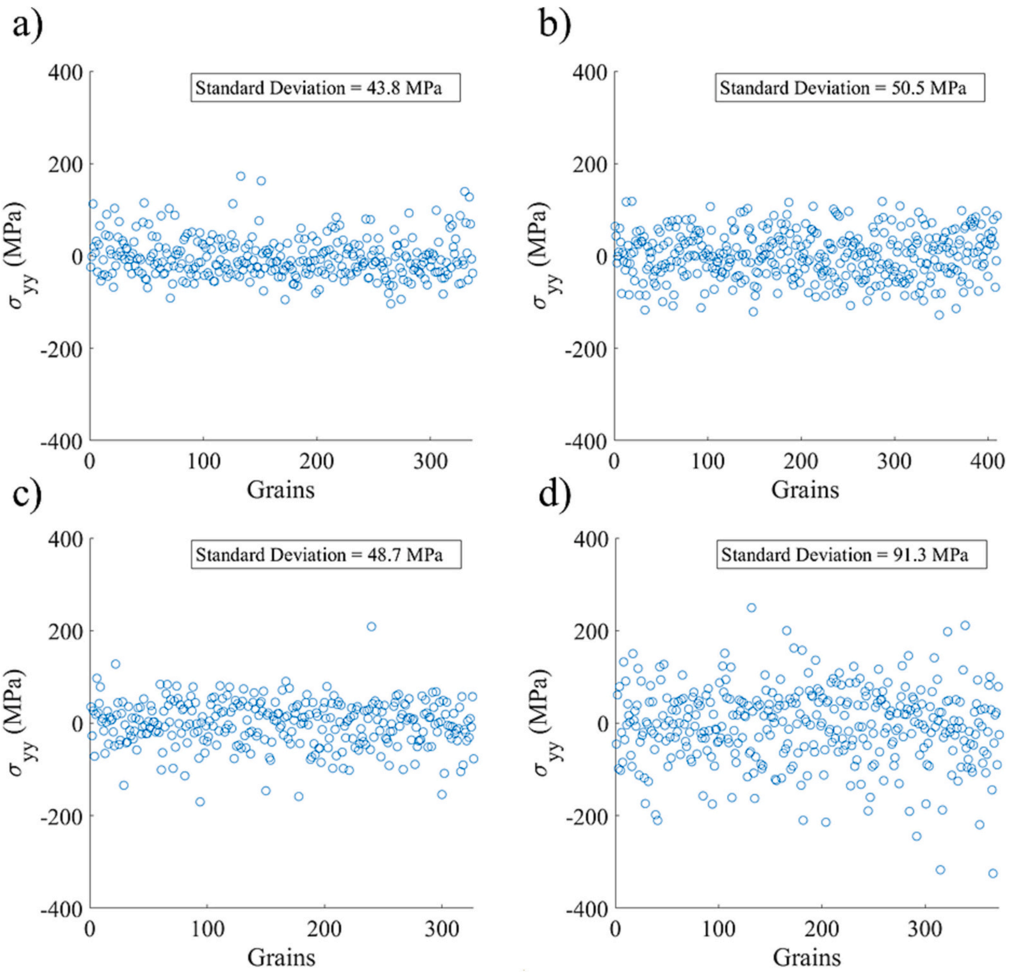

Fig. 9. Grain averaged residual stress along the loading direction in the undeformed state for the a) QS and b) HSR specimens, while c) and d) are in the deformed state for the QS and HSR specimens, respectively.

observed to increase with the degree of applied strain [37], while in the present study, the increased macroscopic stress response of the HSR specimen also resulted in an increased envelope or heterogeneities of residual stress states. FF-HEDM indicates that the HSR specimen had both increased magnitude and heterogeneity of its grain averaged residual stresses as compared to the QS specimen.

A physical rational linking residual stress and lattice reorientation will be constructed here to explain why the HSR specimen was found to hold a larger residual stress distribution than the QS specimen, while its grains demonstrated a lower lattice reorientation after loading. Lattice reorientation can be used as a proxy for local crystallographic slip [38] (crystallographic slip is not directly measurable using diffraction methods). As the barriers preventing dislocation motion are easier to overcome while at load, the longer time spent at load during the QS test (and its intermittent FF scans) likely allowed local plasticity, in the form of lattice reorientation on the grain scale, to occur. Additionally, since crystallographic slip is a strain rate dependent process based on the rate of dislocation generation and annihilation; it is consistent to suggest that increased means of dislocation sinks are required in the QS specimen to facilitate the observed greater lattice reorientation. Grain reorientation has been well studied, particularly in the context of texture evolution from deformation, and it is notable that models, such as the LAMEL model which accounts for this reorientation, incorporate interactions occurring at the grain boundaries [39]. With this in mind, grain boundaries would act as the defect sinks facilitating lattice reorientation, and the QS specimen, with greater lattice reorientation, would then hold a lower dislocation content than the HSR specimen.

Further, in the HSR specimen, it would be expected that the increased spread in the residual stress values and increased macroscopic yield stress of the HSR specimen, would require increased dislocation density content. Grain average residual stress is attributed to the elastic deformation gradient, F^E, which can be measured via FF-HEDM measurements [24]. In the lattice, an incompatible deformation field exists, such that $curl((F^E)^{-1}) = \; curl\,(F^P)$, in which the curl of F^P (F^P being the plastic deformation gradient) is directly attributed to the presence of GNDs via Nye's dislocation tensor [40–42]. Over the years, there have been many studies that have worked to connect the presence of dislocations to residual stresses, c.f. [43–45]. It is postulated here that the subsequent high residual stresses upon unload in the HSR specimen is associated with a greater dislocation content, as seen in past works [13–15], due to the lack of time for dislocation motion during HSR loading to allow for local plasticity through lattice reorientation, as facilitated by grain boundaries acting as defect sinks.

It would then be expected for the EBSD to show a local misorientation difference between the two strain rates, particularly at the grain boundaries; however, intragranular orientation results from EBSD (from which a dislocation density can be derived [46]) shows little to no difference between the strain rates (in general or specifically at grain boundaries). Due to the 2D nature of EBSD only five of the nine components of the Nye dislocation tensor can be determined if the curl of the elastic strain gradient is considered negligible compared to the magnitude of the local lattice rotation; only three if the variations of elastic strains are not negligible [44,46]. With this in mind, a possible explanation for the discrepancy between the starkly different residual stress states of the loading regimes from FF-HEDM (measurements taken in bulk) and lack of intragranular misorientation differences from EBSD (2D surface measurements) is a combination of the subsurface lattice rotations left uncaptured by conventional EBSD and the spatial variations in elastic strain being non-negligible (when the FF-HEDM measurements were taken). Such variations in elastic strains are indicative of intragranular (Type 3) residual stresses and, while this study is unable to indicate the magnitude of the these intragranular variations, Naragani et al. [47] used an incompatible distortion field coupled with FF-HEDM grain averaged strains to determine intragranular strains and demonstrated a large distribution of strains within each grain. Further, as shown by Hayashi et al. [48], grain averaged stresses do not entirely characterize a grain's stress profile and that intragranular stresses, often spatially localized, can deviate as much as the magnitude of the yield stress from the centroid value. Another possibility is that the ability for general Hough-based indexing to distinguish between low levels of dislocation density is limited, with a noise level estimated at $\pm 10^{14}\ m^{-2}$ [49]. In particular, for smaller amounts of deformation, on the order of the 2% total strain as performed in this study, dislocation densities have been shown to be under this noise level in copper [50], and localization at grain boundaries may not be seen in KAM plots without additional deformation [51]. With only 2% total strain imparted to the specimens in this study, the difference between the two strain rates may not be visible in conventional EBSD and as such, differences in the KAM plots would not be expected at the grain boundaries. A final possibility regards the difference in total plastic strain imparted to the two specimens. With a larger plastic strain imparted to the QS specimen (about 2% greater than the HSR specimen), the expected difference in the KAM plot created by a higher strain rate may be overshadowed by the QS specimen's slightly larger total plastic strain and any remaining difference is below the resolution of the Hough-based indexing. However, reduced lattice reorientation is still observed within the HSR specimen from FF-HEDM and the inability for plasticity through lattice reorientation, causing high internal stresses to remain on the grain scale upon unload, remains the most likely mechanism resulting in high magnitudes of Type 2 residual stress.

5. Conclusion

This work investigated the evolution of grain scale residual stresses in SS316L under different applied strain rates (QS at $10^{-4}\ s^{-1}$ and HSR at $10^{2}\ s^{-1}$) and observed that with a higher strain rate came a larger magnitude of Type 2 residual stresses. Additionally, this work demonstrated that for a total strain common to structural engineering applications, the grain averaged reorientation, collected from FF-HEDM, of the QS specimen displayed a larger mean magnitude than the HSR specimen, while the intragranular deformation metrics, namely the KAM and GROD maps as obtained from EBSD, showed no stark differences. Misorientation localization was seen in the GROD plots for both specimens, with deviations up to 2° from the mean orientation. The HSR specimen exhibited a spread in the grain average residual stress values nearly double that of the spread of the QS specimen. The slip system strength is known to be strain rate dependent. Here it is postulated that local plasticity, measured via increased lattice reorientation, facilitated by grain boundaries acting as defect sinks, during the greater time under load in the QS test, resulted in the less extreme values of residual stress. The HSR specimen, with a relatively short loading time, maintained its higher internal stresses upon unload. This work highlights the need for future studies which characterize additional (higher) strain rates to determine if internal residual stresses continue to increase with faster loading as well as explorations into potential dislocation density differences between the strain rates through more angularly resolved techniques.

Declaration of Competing Interest

The authors declare that they have no known competing financial interests or personal relationships that could have appeared to influence the work reported in this paper.

Data availability

The raw/processed data required to reproduce these findings cannot be shared at this time as the data also forms part of an ongoing study.

Acknowledgements

This work was supported by Sandia National Laboratories, under contract number 1701331, as part of the Truman Fellowship Program under the Laboratory Directed Research and Development program at Sandia National Laboratories, as well the National Science Foundation, under grant number CMMI 16–51956. The authors would like to thank Dr. Matthew Hudspeth for providing the specimens, conducting the heat treatment trials, and many informative discussions that shaped the vision of this work. The HEDM characterization was performed at the Cornell High Energy Synchrotron Source (supported by the National Science Foundation under DMR-1829070). The authors would like to thank Priya Ravi for assistance during x-ray data collection, Brandon Mackey for assistance with continuum scale modeling, Dr. Peter Ko for beamline support during the HEDM experiments, and Dr. Kelly Nygren for beamline support, as well as interesting discussions about the HEDM reconstructions.

Sandia National Laboratories is a multimission laboratory managed and operated by National Technology & Engineering Solutions of Sandia, LLC, a wholly owned subsidiary of Honeywell International Inc., for the U.S. Department of Energy's National Nuclear Security Administration under contract DE-NA0003525. This paper describes objective technical results and analysis. Any subjective views or opinions that might be expressed in the paper do not necessarily represent the views of the U.S. Department of Energy or the United States Government.

Appendix A. High Strain Rate Experimental Setup and Displacement Correction

High strain rate tension experiments were conducted using a modified Kolsky tension bar specially designed for this test to allow single loading of a specimen loaded to small strains. A schematic of the setup is shown in Fig. A.1. This design is based on the tubular gun barrel presented by Song et al. [52] but had several modifications, including an impedance matched barrel, multiple momentum bars on the gun barrel side, as well as momentum tubes on the transmission side. The momentum bars, incident bar, and transmission bar were all made from solid 25.4 *mm* diameter 4140 steel. The gun barrel and transmission momentum tubes were also 4140 steel, impedance matched to the 25.4 *mm* diameter solid bars. Prior to the test, a small preset gap (approximately 130 μm) is set between the end cap of the gun barrel and momentum bars. When the striker is fired using compressed gas to impact the end cap, the preset gap closes, bringing the end cap and momentum bars into contact. Meanwhile, a tensile incident pulse is generated that propagates along the barrel and into the incident bar through the coupler. The impedance of the gun barrel is matched to the impedance of the incident bar to minimize disturbance to the incident wave. Now in the incident bar, the incident pulse propagates to the specimen end and pulls the specimen in tension. The wave transmitted through the specimen enters the transmission bar, and propagates to the end of the transmission bar, into the flange, and into the momentum tubes, which are placed in contact prior to the test, bringing the motion of the incident bar to a stop. The reflected compression pulse in the incident bar propagates back to the impact site at the end cap, but since the end cap and momentum bars are in contact, the wave passes into the momentum bars and is trapped, thus stopping the motion of the entire gun barrel and incident bar.

The specimen stress history is calculated using strain gauges mounted on the transmission bar as is typical in Kolsky bar experiments [52].

$$\sigma(t) = \frac{A_0}{A_s} E\varepsilon_t(t) \tag{A.1}$$

Displacement of the grip faces was tracked during the HSR loading using the laser extensometer technique described by Nie et al. [53]. Since the grip displacement was tracked, rather than displacement within the gauge section, a correction was necessary to determine the strain within the gauge section of the specimen. In the past this correction has been determined theoretically, by the geometry of the specimen [54,55]; however, due to the complexity of the geometry in question, a finite element model was constructed in ABAQUS to determine the correction during both the elastic and plastic regime. The correction represents the ratio between the applied displacement that is accommodated by the gauge and the applied displacement that is accommodated by the entire specimen between the grip points.

The 3D specimen model was generated in CAD (Fig. A.2a). Tetrahedral quadratic elements (C3D10) were meshed to the model in ABAQUS. Figs. A.2b,c show the model results from ABAQUS due to the applied loading of similar magnitude to that experienced during the experimental HSR loading. The boundary conditions of the model were identical to those of the specimen during HSR loading: where the X and Z faces of the uppermost and bottommost portions of the grips were on rollers (below and above Nodes 1 and 6 in Fig. A.2a), the bottom Y face was pinned, and displacement was applied to the top Y face. Elastic parameters include the elastic modulus, yield strength, and Poisson ratio: $E = 198\ GPa$, $\sigma_y = 421\ MPa$, $\nu = 0.27$. The modulus and yield point were extracted from the macroscopic loading after the theoretical, correction was applied to the data. The Poisson ratio was assumed to be consistent with commercially available SS316L. Once the yield point was reached, a linear, isotropic hardening rule was implemented in ABAQUS with slope of $1.74x10^3 MPa/\frac{mm}{mm}$. This slope was also extracted from the theoretically corrected stress-strain data of the HSR specimen.

Let all displacements measured during the experiment, specifically displacement along the Y axis, be represented by U, and displacements determined from the FE simulation be called u. The placements of the nodes as shown in Fig. A.2a represent both the vertical location of nodal data extracted from the FE simulation as well as locations of significance during the experiment. The distance between Node 1 and Node 6 represents the distance between the measurement points during the experiment, thus the relative displacement of these two nodes, $U_{Node\ 6} - U_{Node\ 1}$, is used to track the total displacement of the specimen, U_t, or u_t if in terms of u. The distance between Node 2 and Node 5 represents the machined gauge section of 8 *mm*. The distance between Node 3 and Node 4 encloses the region of the gauge section that both contains the interrogation volume of HEDM and has a constant plastic strain during loading in the FE model (Fig. A.2c). For this correction, this shall be considered the working gauge section, has a length of approximately 4.5 *mm*, and the relative displacement of these two nodes, $U_{Node\ 4} - U_{Node\ 3}$, will be called U_g or u_g if in terms of u. The correction, C, as determined by the FE simulation is described by Eq. A.2, where i represents the current displacement step.

$$C^i = \frac{u_g^i - u_g^{i-1}}{u_t^i - u_t^{i-1}} \tag{A.2}$$

The correction, as calculated in Eq. A.2, is constant during elastic loading; this elastic region shall be considered the region up to displacement step $i = a$ with correction C_E. However, once plasticity begins, the correction was found to be dependent on the hardening undergone by the gauge section and is defined by a polynomial expression as a function of the stress beyond the yield stress, $C(\sigma_i - \sigma_y)$. This region, extends from displacement step a to the end of loading, denoted as step $i = b$. To be clear, the correction factor calculated in Eq. A.2 is done with displacement data from the FE model, u, whereas the displacements used in Eq. A.3 to determine the strain within the gauge section of the specimen, is calculated using the displacement data from the experiment, U. Once the corrected displacement was determined, as calculated via Eq. A.3, the corrected strain was calculated with the gauge length defined as the original vertical distance between nodes 3 and 4 (approximately 4.5 *mm* of the full 8 *mm* gauge).

$$U_g = U_t^1 C_E + \sum_{i=2}^{a} \left(U_t^i - U_t^{i-1}\right) C_E + \sum_{i=a+1}^{b} \left(U_t^i - U_t^{i-1}\right) C\left(\sigma_i - \sigma_y\right) \tag{A.3}$$

Fig. A.2d shows the raw, theoretically corrected, and FE corrected stress/strain data. As the raw strain data was calculated assuming all displacement arose from the gauge section, it shows the largest amount of strain. As expected, both the theoretical and FE corrections reduce the strain experienced by the gauge section since the rest of the specimen was allowed to elastically load. Upon plasticizing the two correction factors differ as the FE correction includes hardening, which alters the percentage of displacement, which occurs within the gauge as the stress increases. The corrected final total strain is expected to be 2.03% once an unload, with identical modulus as the initial loading, was applied. The strain rate history was calculated by differentiation of the corrected strain history.

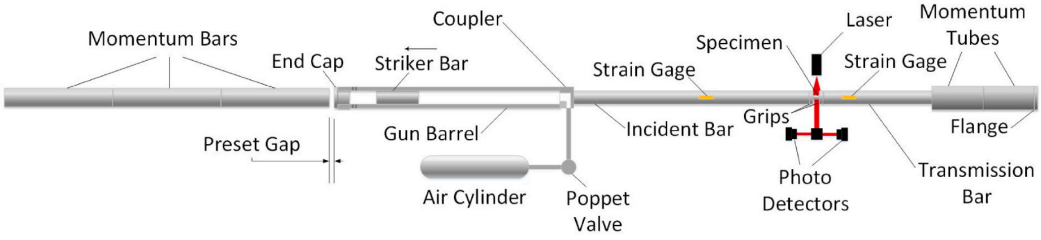

Fig. A.1. Kolsky tension bar design used to apply small strain single loading.

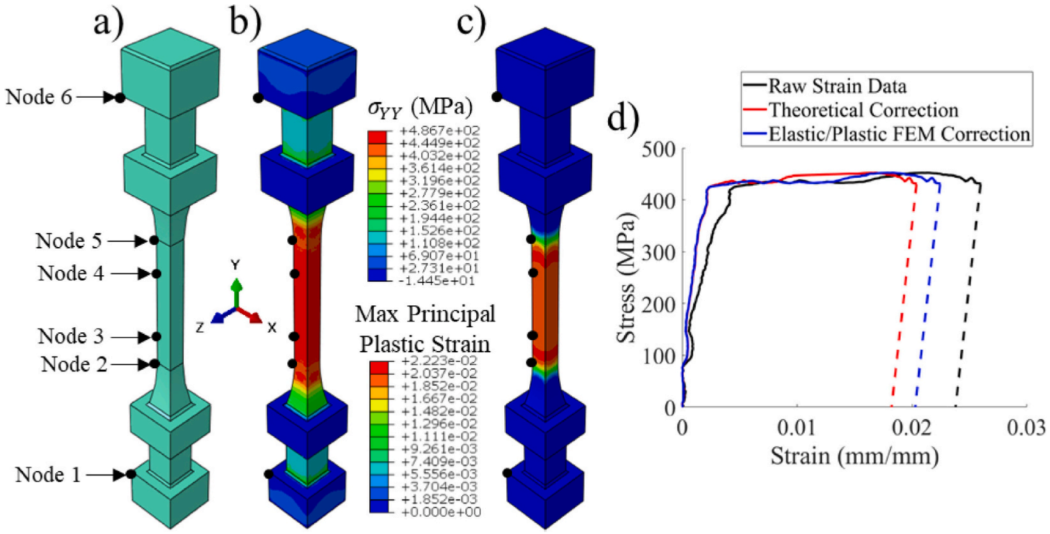

Fig. A.2. FE model results. a) the 3D model, b) the stress along the loading direction, c) the max principal plastic strain, d) comparison of raw, theoretically corrected, and FE corrected stress strain curves. The results shown in both b and c were extracted from the model once plastic strain within the gage section reached the expected conditions applied during the experiment.

Appendix B. Grain Orientation Envelope Analysis

FF-HEDM is a grain averaged technique which uses the centroid positions of each grain's diffraction spots to reconstruct the grain averaged orientation. This orientation represents the most consistent orientation within each grain; the orientation with the highest intensity diffracting volume. However, it is clear from EBSD analysis, as well as investigation of the diffraction spots from FF-HEDM, that there are many other orientations present within a single grain, especially after deformation. Therefore, it is possible to determine all orientations present within a single grain by trialing and thresholding a discrete set of orientations around each centroid orientation. Work by Nygren et al. [56], demonstrates this ability and method on a Ti-7Al polycrystal deformed to approximately 3% strain. The work displays the evolution of a single grain of interest, where it begins in the undeformed state with relatively few orientations within its volume (called a grain orientation envelope (GOE)). Once deformation proceeds, the GOE evolves and expands to encompass many more orientations. These GOEs neatly display what is also shown in the GROD plots from EBSD, that there are many more orientations present within a single grain than the average or centroid orientation.

Using this methodology, a grain from each specimen, QS and HSR, were chosen for their relative similar size, and that they both exist within a single FF-HEDM diffraction volume in their respective specimens. For each grain, a discrete volume of orientation space was created, centered about the grain averaged orientation. These orientations were then trialed as done by Nygren et al. for both the undeformed and deformed states; orientations with completeness of 1.0 were extracted. The findings were then plotted in Rodriguez space as shown in Fig. B.1a-d. Fig. B.1a,b shows the evolution of the QS grain such that it begins with very few orientations and, with deformation, expands drastically. Fig. B.1e shows a cumulative distribution function (CDF) of the misorientation in the deformed state of the GOE to the deformed grain averaged orientation. This shows that this grain contains orientations with misorientation as great as 3° from the grain averaged orientation. Similar plots are shown for the HSR specimen in Fig. B.1c,d,f, with the CDF demonstrating an internal possible misorientation of approximately 2.5°. Fig. B.1c demonstrates a slightly larger undeformed GOE in its HSR grain as compared the QS grain. This is attributed to different experimental x-ray conditions (specifically x-ray optics) rather than a difference in original microstructure, as all three beamtimes (undeformed HSR, deformed HSR, and QS) were performed in different experimental hutches. These two plots clearly demonstrate that grains within both specimens deform to such an extent that misorientations of at least 2° exist. The greater spread in misorientation seen from the GOEs, as compared to the GROD plots, is due to a combination of FF-HEDM's higher orientation resolution than conventional EBSD and the ability for FF-HEDM to capture the full 3D grain in bulk instead of a single 2D slice.

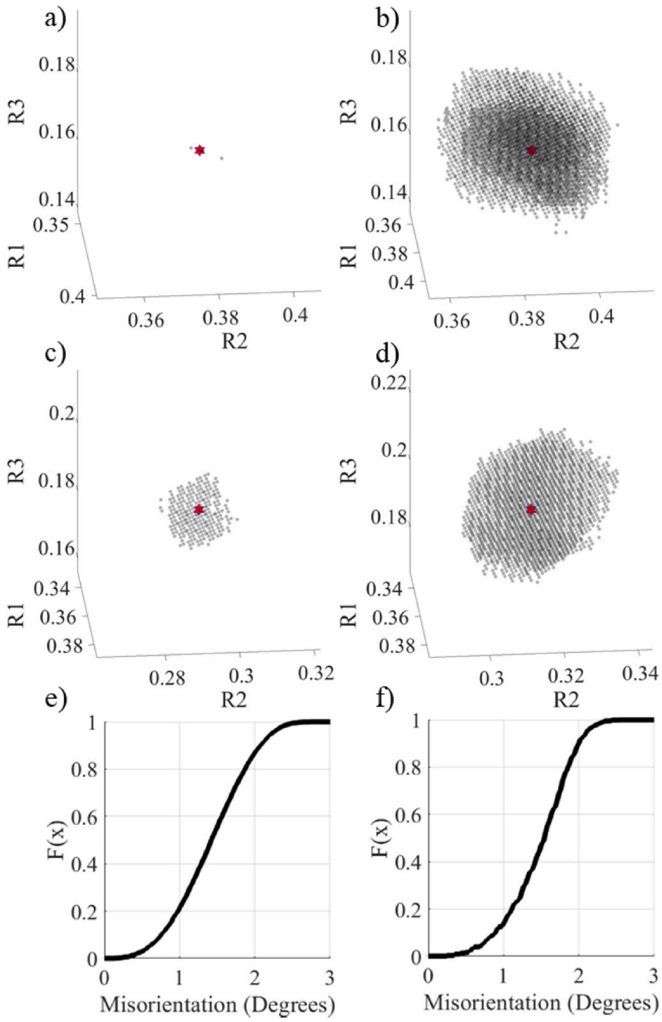

Fig. B.1. Grain orientation envelope (GOE) in the initial, undeformed state for the a) QS and, c) HSR specimens. GOE in the final, deformed state for the b) QS and, d) HSR specimens. Cumulative distribution function of misorientation of the deformed GOE from the deformed centroid orientation for the e) QS and, f) HSR specimens. The stars indicate the grain's centroid orientation.

References

[1] C. Zener, J.H. Hollomon, Effect of strain rate upon plastic flow of steel, J. Appl. Phys. 15 (1944) 22–32, https://doi.org/10.1063/1.1707363.

[2] R.W. Armstrong, S.M. Walley, High strain rate properties of metals and alloys, Int. Mater. Rev. 53 (2008) 105–128, https://doi.org/10.1179/174328008X277795.

[3] W.S. Lee, C.F. Lin, T.J. Liu, Impact and fracture response of sintered 316L stainless steel subjected to high strain rate loading, Mater. Charact. 58 (2007) 363–370, https://doi.org/10.1016/j.matchar.2006.06.004.

[4] R. Othman, P. Guégan, G. Challita, F. Pasco, D. LeBreton, A modified servo-hydraulic machine for testing at intermediate strain rates, Int. J. Impact Eng. 36 (2009) 460–467, https://doi.org/10.1016/j.ijimpeng.2008.06.003.

[5] B. Song, B. Sanborn, J.D. Heister, R.L. Everett, T.L. Martinez, G.E. Groves, E. P. Johnson, D.J. Kenney, M.E. Knight, M.A. Spletzer, K.K. Haulenbeek, C. McConnell, An apparatus for tensile characterization of materials within the upper intermediate strain rate regime, Exp. Mech. 59 (2019) 941–951, https://doi.org/10.1007/s11340-019-00494-3.

[6] H. Kolsky, An investigation of the mechanical properties of materials at very high rates of loading, Proc. Phys. Soc. Sect. B. 62 (1949) 676–700, https://doi.org/10.1088/0370-1301/62/11/302.

[7] W. Chen, B. Song, Split Hopkinson (Kolsky) Bar, Springer US, Boston, MA, 2011, https://doi.org/10.1007/978-1-4419-7982-7.

[8] M. Isakov, S. Hiermaier, V.-T. Kuokkala, Improved specimen recovery in tensile split Hopkinson bar, Philos. Trans. R. Soc. A Math. Phys. Eng. Sci. 372 (2014) 20130194, https://doi.org/10.1098/rsta.2013.0194.

[9] W.S. Lee, C.F. Lin, Impact properties and microstructure evolution of 304l stainless steel, Mater. Sci. Eng. A 308 (2001) 124–135, https://doi.org/10.1016/S0921-5093(00)02024-4.

[10] A. Kundu, D.P. Field, P. Chandra Chakraborti, Effect of strain and strain rate on the development of deformation heterogeneity during tensile deformation of a solution annealed 304 LN austenitic stainless steel: an EBSD study, Mater. Sci. Eng. A 773 (2020), 138854, https://doi.org/10.1016/j.msea.2019.138854.

[11] S. Acharya, A. Moitra, S. Bysakh, M. Nanibabu, S.A. Krishanan, C. K. Mukhopadhyay, K.V. Rajkumar, G. Sasikala, A. Mukhopadhyay, D.K. Mondal, K. S. Ghosh, B.B. Jha, K. Muraleedharan, Effect of high strain rate deformation on the properties of SS304L and SS316LN alloys, Mech. Mater. 136 (2019), 103073, https://doi.org/10.1016/j.mechmat.2019.103073.

[12] M.D. Sangid, The physics of fatigue crack initiation, Int. J. Fatigue 57 (2013) 58–72, https://doi.org/10.1016/j.ijfatigue.2012.10.009.

[13] P.S. Follansbee, U.F. Kocks, A constitutive description of the deformation of copper based on the use of the mechanical threshold stress as an internal state variable, Acta Metall. 36 (1988) 81–93, https://doi.org/10.1016/0001-6160(88)90030-2.

[14] F.J. Zerilli, R.W. Armstrong, The effect of dislocation drag on the stress-strain behavior of F.C.C. metals, Acta Metall. 40 (1992) 1803–1808, https://doi.org/10.1016/0956-7151(92)90166-C.

[15] H. Jin, B. Sanborn, W.Y. Lu, B. Song, Mechanical characterization of 304L-VAR stainless steel in tension with a full coverage of low, intermediate, and high strain rates, Mech. Mater. 152 (2021), https://doi.org/10.1016/j.mechmat.2020.103654.

[16] P.J. Withers, H.K.D.H. Bhadeshia, Residual stress. Part 1 – Measurement techniques, Mater. Sci. Technol. 17 (2001) 355–365, https://doi.org/10.1179/026708301101509980.

[17] P.J. Withers, H.K.D.H. Bhadeshia, Residual stress. Part 2 – nature and origins, Mater. Sci. Technol. 17 (2001) 366–375, https://doi.org/10.1179/026708301101510087.

[18] P. Peyre, X. Scherpereel, L. Berthe, C. Carboni, R. Fabbro, G. Béranger, C. Lemaitre, Surface modifications induced in 316L steel by laser peening and shot-peening. Influence on pitting corrosion resistance, Mater. Sci. Eng. A 280 (2000) 294–302, https://doi.org/10.1016/S0921-5093(99)00698-X.

[19] O. Takakuwa, H. Soyama, Effect of residual stress on the corrosion behavior of austenitic stainless steel, Adv. Chem. Eng. Sci. 05 (2015) 62–71, https://doi.org/10.4236/aces.2015.51007.

[20] H. Poulsen, Three-Dimensional X-Ray Diffraction Microscopy, Springer, Berlin Heidelberg, Berlin, Heidelberg, 2004, https://doi.org/10.1007/b97884.

[21] J. Oddershede, S. Schmidt, H.F. Poulsen, H.O. Sørensen, J. Wright, W. Reimers, Determining grain resolved stresses in polycrystalline materials using three-dimensional X-ray diffraction, J. Appl. Crystallogr. 43 (2010) 539–549, https://doi.org/10.1107/S0021889810012963.

[22] N.Y. Juul, G. Winther, D. Dale, M.K.A. Koker, P. Shade, J. Oddershede, Elastic interaction between twins during tensile deformation of austenitic stainless steel, Scr. Mater. 120 (2016) 1–4, https://doi.org/10.1016/j.scriptamat.2016.03.022.

[23] K. Chatterjee, A. Venkataraman, T. Garbaciak, J. Rotella, M.D. Sangid, A. J. Beaudoin, P. Kenesei, J.S. Park, A.L. Pilchak, Study of grain-level deformation and residual stresses in Ti-7Al under combined bending and tension using high energy diffraction microscopy (HEDM), Int. J. Solids Struct. 94–95 (2016) 35–49, https://doi.org/10.1016/j.ijsolstr.2016.05.010.

[24] K. Kapoor, M.D. Sangid, Initializing type-2 residual stresses in crystal plasticity finite element simulations utilizing high-energy diffraction microscopy data, Mater. Sci. Eng. A 729 (2018) 53–63, https://doi.org/10.1016/j.msea.2018.05.031.

[25] A.K. Tiwari, A.R. Patel, N. Kumar, Investigation of strain rate on residual stress distribution, Mater. Des. 65 (2015) 1041–1047, https://doi.org/10.1016/j.matdes.2014.09.051.

[26] P.A. Shade, B. Blank, J.C. Schuren, T.J. Turner, P. Kenesei, K. Goetze, R.M. Suter, J. V. Bernier, S.F. Li, J. Lind, U. Lienert, J. Almer, A rotational and axial motion system load frame insert for in situ high energy x-ray studies, Rev. Sci. Instrum. 86 (2015), 093902, https://doi.org/10.1063/1.4927855.

[27] R.M. Suter, D. Hennessy, C. Xiao, U. Lienert, Forward modeling method for microstructure reconstruction using x-ray diffraction microscopy: single-crystal verification, Rev. Sci. Instrum. 77 (2006) 1–12, https://doi.org/10.1063/1.2400017.

[28] J.V. Bernier, N.R. Barton, U. Lienert, M.P. Miller, Far-field high-energy diffraction microscopy: a tool for intergranular orientation and strain analysis, J. Strain Anal. Eng. Des. 46 (2011) 527–547, https://doi.org/10.1177/0309324711405761.

[29] R.C. Hurley, E.B. Herbold, D.C. Pagan, Characterization of the crystal structure, kinematics, stresses and rotations in angular granular quartz during compaction, J. Appl. Crystallogr. 51 (2018) 1021–1034, https://doi.org/10.1107/S1600576718006957.

[30] H.M. Ledbetter, Stainless-steel elastic constants at low temperatures, J. Appl. Phys. 52 (1981) 1587–1589, https://doi.org/10.1063/1.329644.

[31] D.C. Pagan, J.V. Bernier, D. Dale, J.Y.P. Ko, T.J. Turner, B. Blank, P.A. Shade, Measuring Ti-7Al slip system strengths at elevated temperature using high-energy X-ray diffraction, Scr. Mater. 142 (2018) 96–100, https://doi.org/10.1016/j.scriptamat.2017.08.029.

[32] F. Bachmann, R. Hielscher, H. Schaeben, Texture analysis with MTEX – free and open source software toolbox, Solid State Phenom. 160 (2010) 63–68, https://doi.org/10.4028/www.scientific.net/SSP.160.63.

[33] S.I. Wright, M.M. Nowell, D.P. Field, A review of strain analysis using Electron backscatter diffraction, Microsc. Microanal. 17 (2011) 316–329, https://doi.org/10.1017/S1431927611000055.

[34] R.J. Asaro, Crystal plasticity, J. Appl. Mech. 50 (1983) 921–934, https://doi.org/10.1115/1.3167205.

[35] A. Das, S. Tarafder, S. Sivaprasad, D. Chakrabarti, Influence of microstructure and strain rate on the strain partitioning behaviour of dual phase steels, Mater. Sci. Eng. A 754 (2019) 348–360, https://doi.org/10.1016/j.msea.2019.03.084.

[36] K.E. Nygren, D.C. Pagan, J.V. Bernier, M.P. Miller, An algorithm for resolving intragranular orientation fields using coupled far-field and near-field high energy X-ray diffraction microscopy, Mater. Charact. 165 (2020), 110366, https://doi.org/10.1016/j.matchar.2020.110366.

[37] M.D. Sangid, J. Rotella, D. Naragani, J.-S. Park, P. Kenesei, P.A. Shade, A complete grain-level assessment of the stress-strain evolution and associated deformation response in polycrystalline alloys, Acta Mater. 201 (2020) 36–54, https://doi.org/10.1016/j.actamat.2020.09.051.

[38] D.C. Pagan, K.E. Nygren, M.P. Miller, Analysis of a three-dimensional slip field in a hexagonal Ti alloy from in-situ high-energy X-ray diffraction microscopy data, Acta Mater. 221 (2021), 117372, https://doi.org/10.1016/j.actamat.2021.117372.

[39] P. Van Houtte, S. Li, M. Seefeldt, L. Delannay, Deformation Texture Prediction: From the Taylor Model to the Advanced Lamel Model, 2005, https://doi.org/10.1016/j.ijplas.2004.04.011.

[40] A. Arsenlis, D. Parks, Crystallographic aspects of geometrically-necessary and statistically-stored dislocation density, Acta Mater. 47 (1999) 1597–1611, https://doi.org/10.1016/S1359-6454(99)00020-8.

[41] A. Acharya, J.L. Bassani, Lattice incompatibility and a gradient theory of crystal plasticity, J. Mech. Phys. Solids. 48 (2000) 1565–1595, https://doi.org/10.1016/S0022-5096(99)00075-7.

[42] S. Das, F. Hofmann, E. Tarleton, Consistent determination of geometrically necessary dislocation density from simulations and experiments, Int. J. Plast. 109 (2018) 18–42, https://doi.org/10.1016/j.ijplas.2018.05.001.

[43] E. Kröner, On the physical reality of torque stresses in continuum mechanics, Int. J. Eng. Sci. 1 (1963) 261–278, https://doi.org/10.1016/0020-7225(63)90037-5.

[44] A.J. Wilkinson, E.E. Clarke, T.B. Britton, P. Littlewood, P.S. Karamched, High-resolution electron backscatter diffraction: an emerging tool for studying local deformation, J. Strain Anal. Eng. Des. 45 (2010) 365–376, https://doi.org/10.1243/03093247JSA587.

[45] J. Jiang, T.B. Britton, A.J. Wilkinson, Measurement of geometrically necessary dislocation density with high resolution electron backscatter diffraction: effects of detector binning and step size, Ultramicroscopy. 125 (2013) 1–9, https://doi.org/10.1016/j.ultramic.2012.11.003.

[46] W. Pantleon, Resolving the geometrically necessary dislocation content by conventional electron backscattering diffraction, Scr. Mater. 58 (2008) 994–997, https://doi.org/10.1016/j.scriptamat.2008.01.050.

[47] D. Naragani, P. Shade, W. Musinski, D. Boyce, M. Obstalecki, D. Pagan, J. Bernier, A. Beaudoin, Interpretation of intragranular strain fields in high-energy synchrotron X-ray experiments via finite element simulations and analysis of incompatible deformation, Mater. Des. 210 (2021), 110053, https://doi.org/10.1016/j.matdes.2021.110053.

[48] Y. Hayashi, D. Setoyama, Y. Hirose, T. Yoshida, H. Kimura, Intragranular three-dimensional stress tensor fields in plastically deformed polycrystals, Science (80-.) 366 (2019) 1492–1496, https://doi.org/10.1126/science.aax9167.

[49] A.J. Wilkinson, D. Randman, Determination of elastic strain fields and geometrically necessary dislocation distributions near nanoindents using electron back scatter diffraction, Philos. Mag. 90 (2010) 1159–1177, https://doi.org/10.1080/14786430903304145.

[50] J. Jiang, T. Ben Britton, A.J. Wilkinson, Accumulation of geometrically necessary dislocations near grain boundaries in deformed copper, Philos. Mag. Lett. 92 (2012) 580–588, https://doi.org/10.1080/09500839.2012.700412.

[51] P. Chen, S.C. Mao, Y. Liu, F. Wang, Y.F. Zhang, Z. Zhang, X.D. Han, In-situ EBSD study of the active slip systems and lattice rotation behavior of surface grains in aluminum alloy during tensile deformation, Mater. Sci. Eng. A 580 (2013) 114–124, https://doi.org/10.1016/j.msea.2013.05.046.

[52] B. Song, B.R. Antoun, K. Connelly, J. Korellis, W.-Y. Lu, Improved Kolsky tension bar for high-rate tensile characterization of materials, Meas. Sci. Technol. 22 (2011), 045704, https://doi.org/10.1088/0957-0233/22/4/045704.

[53] X. Nie, B. Song, C.M. Loeffler, A novel splitting-beam laser extensometer technique for Kolsky tension Bar experiment, J. Dyn. Behav. Mater. 1 (2015) 70–74, https://doi.org/10.1007/s40870-015-0005-7.

[54] B. Song, P.E. Wakeland, M. Furnish, Dynamic tensile characterization of Vascomax® Maraging C250 and C300 alloys, J. Dyn. Behav. Mater. 1 (2015) 153–161, https://doi.org/10.1007/s40870-015-0016-4.

[55] B. Song, B. Sanborn, D. Susan, K. Johnson, J. Dabling, J. Carroll, A. Brink, S. Grutzik, A. Kustas, Correction of specimen strain measurement in Kolsky tension bar experiments on work-hardening materials, Int. J. Impact Eng. 132 (2019), 103328, https://doi.org/10.1016/j.ijimpeng.2019.103328.

[56] K.E. Nygren, D.C. Pagan, M.P. Miller, Sub-grain orientation resolution during continuous loading using only far-field HEDM, IOP Conf. Ser. Mater. Sci. Eng. 580 (2019), 012018, https://doi.org/10.1088/1757-899X/580/1/012018.